Computational Analysis of Shrouded Wind Turbine Configurations

Aniket C. Aranake* Vinod K. Lakshminarayan† Karthik Duraisamy ‡

Computational analysis of diffuser-augmented turbines is performed using high resolution computations of the Reynolds Averaged Navier–Stokes equations supplemented with a transition model. Shroud geometries, generated by the extrusion of airfoil profiles into annular wings, are assessed based on their ability to capture mass-flow through the interior of the shroud. To this end, axisymmetric calculations of high-lift airfoil sections are performed. The amplification of mass flow through a shroud is found to increase nearly linearly with radial lift force, and nonlinear effects are examined in terms of the location of the leading edge stagnation point. Of the shapes considered, the Selig S1223 high-lift low-Re airfoil is found to best promote mass flow rate. Following this, full three-dimensional simulations of shrouded wind turbines are performed for selected shroud geometries. The results are compared to bare turbine solutions. Augmentation ratios (defined as the ratio of the power generated by a shrouded turbine to the Betz limit) of up to 1.9 are achieved by the shrouded turbines. Peak augmentation occurs at the highest wind speed for which the flow over the bare turbine blade stays attached. Flow fields are examined in detail and the following aspects are investigated: regions with flow separation, the development of averaged velocity profiles, and the interaction between the helical turbine wake and shroud boundary layer. Finally, power augmentation is demonstrated to continue increasing at high wind velocities, at which the turbine blade would otherwise stall, if a constant tip speed ratio is maintained.

Nomenclature

α	Shroud angle of attack
$\dot{m}$	Mass flow rate
λ	Tip speed ratio, $\frac{\omega R}{U_\infty}$
ω	Turbine angular velocity
ϕ	Blade twist
ρ	Density
c	Shroud chord length
c_f	Skin friction coefficient
C_P	Turbine power coefficient, $P/\frac{1}{2}\rho V_o^3 \pi R^2$
C_p	Pressure coefficient
C_r	Shroud radial force coefficient, $\vec{F}\cdot\hat{r}/\rho U_\infty^2$
C_T	Turbine thrust coefficient, $T/\rho\pi R^2 V_{tip}^2$
$C_{P,b}$	Power coefficient for bare turbine
$C_{P,d}$	Power coefficient for turbine with diffuser
M_∞	Freestream Mach number
M_r	Mass flow amplification factor, $\dot{m}/\rho U_\infty \pi R_s^2$
p	Local field pressure
p_∞	Freestream pressure
R	Turbine radius

*PhD Candidate, Department of Aeronautics and Astronautics, Stanford University, Stanford, CA.
†Postdoctoral Fellow, Department of Aeronautics and Astronautics, Stanford University, Stanford, CA.
‡Assistant Professor (Consulting), Department of Aeronautics and Astronautics, Stanford University, Stanford, CA.

r	Radial coordinate
r_a	Augmentation ratio, $C_P/0.593$
R_s	Shroud radius
Re	Reynolds number, $\rho U_\infty R/\mu$
T	Turbine thrust
U_∞	Freestream velocity
u_z	Axial component of velocity
V_{tip}	Turbine tip velocity, ωR
z	Axial coordinate

I. Introduction

The efficiency of conventional horizontal axis wind turbines is limited by the well-known Betz limit, which states that the maximum amount of power a turbine may extract is equal to 59.3% of the power available in the wind in a streamtube with an area equal to that swept by the rotor. It has also long been theorized, however, that improvements in efficiency beyond this limit can be achieved by placing the turbine inside a shroud which is designed to accelerate the wind before passing it through the turbine. The power available in wind is proportional to the cube of velocity, so small accelerations to the air lead to large increases in potential power extraction. A turbine augmented in this way is often referred to as a diffuser augmented wind turbine (DAWT) or a shrouded wind turbine.

The idea of a DAWT was first proposed by Lilley and Rainbird.[1] Experimental investigations were performed in the 1980s by Gilbert and Foreman[2] and by Igra,[3] both of whom also developed simple low-order models to predict the power augmentation of a DAWT. Although these experiments did demonstrate that power extraction beyond the classic Betz limit is possible, the DAWT was determined not to be profitable compared to traditional wind turbines and was not pursued extensively. Recently however, an increasing number of publications on the topic and high-profile attempts to commercialize the idea indicate a renewed interest in DAWTs. An investigation by Hansen[4] demonstrates using both low-fidelity momentum theory and CFD that the power augmentation of a DAWT is proportional to the increase in mass flow rate through the turbine blades. Additional theoretical advancements which include corrections to the models originally proposed by Gilbert et al.[2] and Igra[3] have been developed by Werle and Presz.[5] A generalized version of the classic Betz limit has been proposed by Jamieson,[6] who claims the maximum power extractable from a wind turbine with augmentation is 8/9ths of the power available in the streamtube which passes through the swept blade area. Throughout the past decade, Abe and Ohya[7,8] have done extensive experimental and computational work on this topic which has led to the development of a high performance so-called "flanged diffuser". A survey including a comprehensive history of DAWTs has been recently published by van Bussel.[9]

Frequently in the study of shrouded turbines, the actuator disk assumption is used to model the turbine blades. In this model, the rotor is replaced by an infinitely thin disk across which a pressure drop is explicitly imposed. This simplification offers a substantial cost saving over a full three-dimensional solution, making it a useful tool during the preliminary design stage. It does not, however, capture potentially interesting aspects of the flow physics near the blade and in the wake of a shrouded turbine. In addition, the actuator disk model cannot predict the effect of the turbine wake on flow separation along the walls of the shroud. This effect, the "swirl mixing mechanism" mentioned in previous literature,[2] has potentially significant consequences on the performance of a DAWT.

An additional complication to the modelling of wind turbine systems is that free transition from laminar to turbulent flow, which occurs on wind turbine blades during typical operating conditions, is found to significantly impact both pressure and viscous forces. Recently, authors of the present work have performed a detailed validation of 3D simulations of an open wind turbine[10] using the $\gamma - \overline{Re_{\theta t}} - SA$ transition model,[11] which is demonstrated to accurately predict transitional flows in two and three dimensions. The solver has also been validated previously by Lakshminarayan and Baeder[12] for the analysis of microscale shrouded rotorcraft aerodynamics.

The present work employs this previously validated methodology to examine shrouded wind turbines. Section II outlines the high-order overset methodology used in this work. In section III, axisymmetric computations are performed to establish a relationship between the aerodynamic force on a shroud and the mass flow rate through its interior. Based on this analysis, a high-lift airfoil shape is selected for detailed investigation. In Section IV, analysis of 3D shrouded wind turbines is discussed. A substantial augmentation

in power is achieved by the introduction of a simple shroud, and considerably greater gains in performance are attained with the use of a high-lift airfoil as the shroud cross sectional profile. Visualizations of the flow field around the blade and the shroud are presented and the flow features are examined in detail.

II. Methodology

In this work, computations are performed using the overset structured mesh solver OVERTURNS.[13] This code solves the compressible RANS equations using a preconditioned dual-time scheme in the diagonalized approximate factorization framework, described by Buelow et al.[14] and Pandya et al.[15] The diagonal form of the implicit approximate factorization method was originally developed by Pulliam and Chaussee.[16] Low Mach preconditioning, based on that developed by Turkel,[17] is used not only to improve convergence, but also to improve the accuracy of the spatial discretization. Inviscid terms are computed using a third order MUSCL scheme utilizing Koren's limiter with Roe's flux difference splitting, and the viscous terms are computed using second order central differencing. For RANS closure, the Spalart-Allmaras[18] turbulence model is employed. To capture the effects of flow transition, the $\gamma - \overline{RE_{\theta t}} - SA$[10,11] model is used.

An implicit hole-cutting technique developed by Lee[19] and improved by Lakshminarayan[13] is used to determine the connectivity information between various overset meshes. For each axisymmetric calculation, the grid system consists of a rectangular background mesh and a single airfoil mesh which represents a shroud. In three dimensions, body conforming meshes for the shroud and turbine blade are embedded in a semi-cylindrical background mesh with periodic boundary conditions. The RANS equations are solved in the rotational frame, with no-slip conditions accounting for wall velocities applied on the surfaces of both the shroud and turbine blade.

III. Analysis of Shroud Airfoil Sections

Early work attempted to model the behavior of a shrouded wind turbine as an internal flow problem,[2,3] in which a turbine was placed inside a duct with an imposed pressure condition at the duct outlet. More recently, however, it has been determined[5,6] that this assumption is inaccurate, and a more appropriate boundary condition is one which is imposed far downstream of the entire system, i.e., the shrouded turbine must be treated as an external flow problem. It is in light of this that the present work treats a shroud as an airfoil extruded axisymmetrically into an annular wing. This permits a preliminary examination of a variety of shroud shapes via relatively inexpensive flow solutions.

A. Inviscid effect of shroud dimension

The geometry of the problem under consideration is shown in Figure 1a. The shroud radius R_s is defined as the distance from the centerline to the shroud at the axial location where the turbine is located. This axial location is selected as 10% of the shroud chord length c. The radial force coefficient is defined as

$$C_r = \frac{\oint_S p\hat{n}dS \cdot \hat{r}}{\frac{1}{2}\rho U_\infty^2} \tag{1}$$

where P is pressure, $\hat{n}$ is a unit normal to the airfoil surface, S is a closed curve defining the airfoil surface, $\hat{r}$ is a unit vector in the radial direction, ρ is the density of air, and U_∞ is the freestream velocity.

To investigate the effect of shroud radius on radial force, a series of two-dimensional grids were generated using NACA0006 airfoil sections with angles of attack varying from $\alpha = 0^\circ$ to $\alpha = 15^\circ$. The radius of the shroud is varied from $R_s = 1$ to $R_s = 7$. Structured overset meshes are used, with 267×51 points in the airfoil mesh in the wrap-around and normal direction respectively and a minimum of 120×90 points in the rectangular background meshes, which were tailored to each shroud radius.

Figure 1b depicts the radial force as a function of angle of attack for a NACA0006 airfoil at various values of R_s/c. The limiting curve for $R_s \to \infty$ is the result of 2D thin airfoil theory. The sign of this force is negative, indicating that the pressure over the airfoil is higher on the outer surface of the shroud than the inner surface, and the shroud structure experiences an aerodynamic force compressing it towards the centerline. The magnitude of the force is much greater for low values of R_s/c, particularly at high angles, and especially large gains are seen by reducing this ratio to below 2. Thus, in order to attain a greater force,

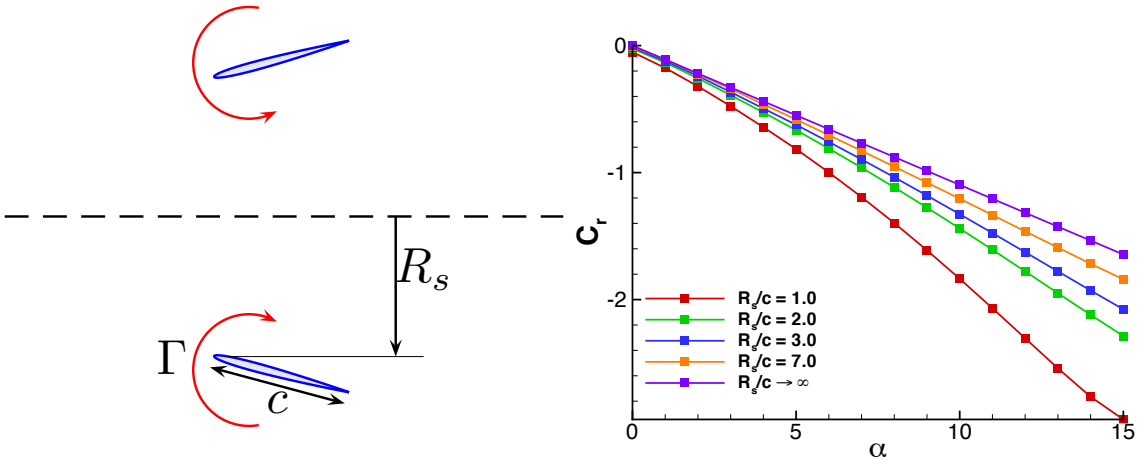

(a) Shroud geometry. Circulation draws air through the inside of the diffuser.

(b) Inviscid radial force

Figure 1: Schematic and radial force behavior of an inviscid shroud with NACA0006 cross section

a low R_s/c is desirable. As a practical consideration, this indicates that the benefit of introducing a shroud to a wind turbine is more easily realized for small turbines, where a low R_s/c ratio is feasible.

B. Exploration of airfoil geometry

One measure of the effectiveness of an airfoil as a shroud profile is the amount of mass flow it induces through the interior of the shroud. The Kutta-Joukowksi theorem states that the lift per span of an airfoil is proportional to the circulation it induces in the surrounding flow. For an axisymmetric shroud, a large circulation corresponds to to a large mass flow rate. The mass flow rate is given by

$$\dot{m} = \int_0^{2\pi} \int_0^{R_s} \rho u_z r dr d\theta \tag{2}$$

where u_z is the axial component of velocity. A non-dimensional mass flow amplification factor is defined as

$$M_r = \frac{\dot{m}}{\rho U_\infty \pi R_s^2}. \tag{3}$$

As an initial investigation of shroud geometries, several high-lift airfoils are considered. The selected shapes are each shown alongside a NACA0006 profile in Figure 2a. The Eppler E423[20] is an airfoil designed to maximize lift through the use of a concave pressure recovery with no specific regard to the effect on moment coefficient. The modified NACA0006 was generated by rotating the mean camber line downward by 45° for the last 20% of the chord length while maintaining the original thickness distribution. This shape is intended to resemble an airfoil with a deflected control surface, and it also approximates the flanged diffuser shape of Abe and Ohya.[7,8] The Selig S1223 is designed with the same high-lift design philosophy as the Eppler E423,[20] and is intended to belong to the FX CL/MS-class of airfoils. The FX 74-CL4-140 is a high-lift airfoil designed for a Reynolds number of $Re = 10^6$.

Two-dimensional overset grids are used for these computations, with 180×218 points in the background mesh and 267×61 points in the near-body mesh. A sample grid of an S1223 section at 10° angle of attack is shown in Figure 3. The Reynolds number based on shroud length is $Re = 3.2 \times 10^6$, corresponding to a freestream velocity of 10 m/s and shroud length of 5.029 m. The axisymmetric RANS equations are solved along with the Spalart-Allmaras turbulence model. The background mesh is extended to 25 chord lengths upstream, 25 chord lengths laterally, and 50 chord lengths downstream. A small value of $r = 0.001$ m is used at the boundary near the symmetry axis, where an extrapolation boundary condition is applied.

The computed performance of these airfoils in terms of radial force and mass flow is shown in Figure 2b. The mass flow amplification is seen to increase nearly linearly with radial force coeffcient. This agrees with

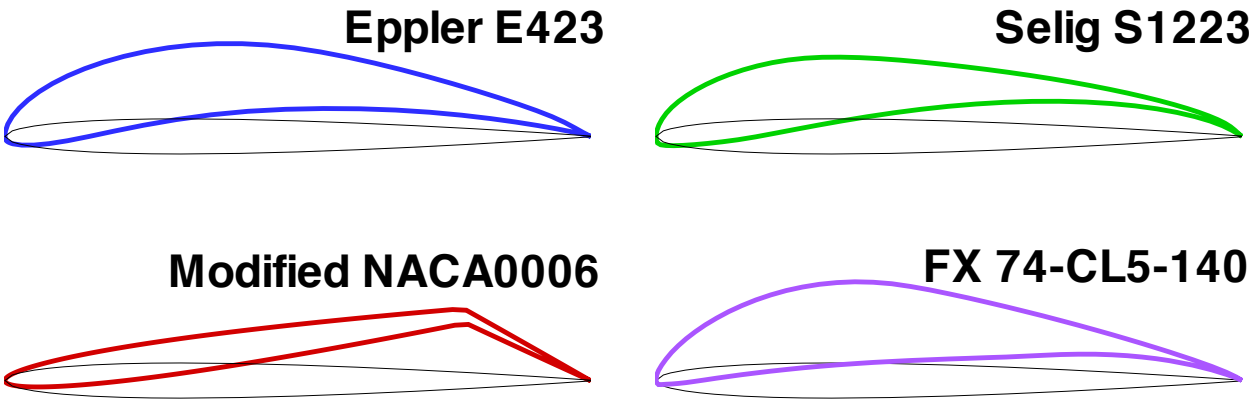

(a) Airfoil shapes

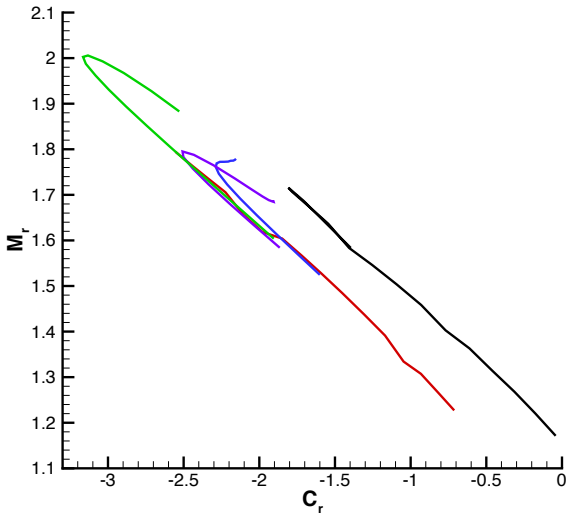

(b) Mass flow amplification M_r vs. radial force coefficient C_r

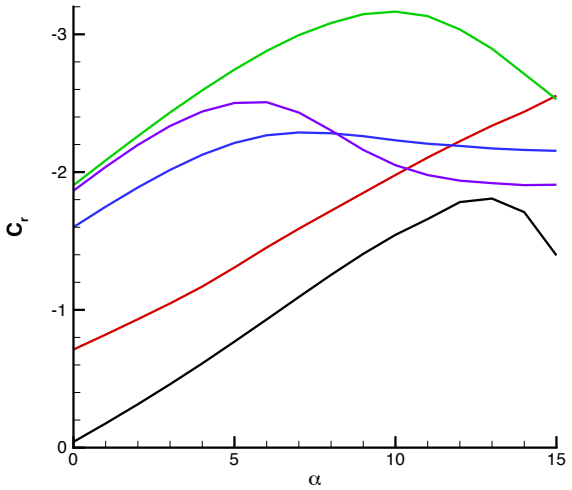

(c) Radial force coefficient C_r vs. angle of attack α

Figure 2: High-lift sections shapes and performance, black lines are NACA0006

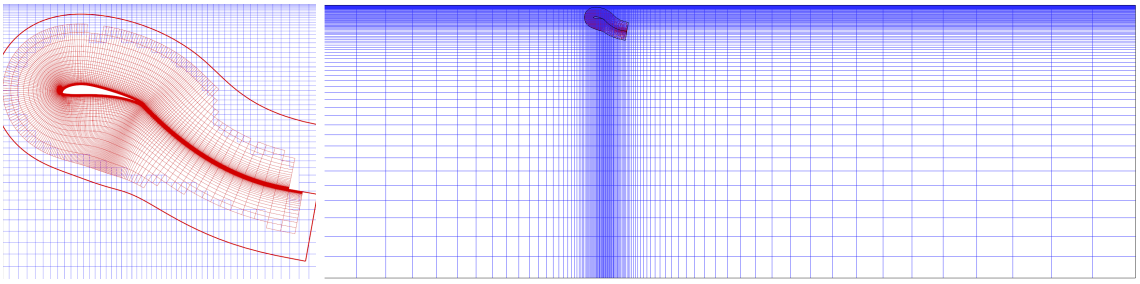

(a) Airfoil grid

(b) Background grid

Figure 3: Overset grid system used for viscous axisymmetric computations

the schematic depicted in Figure 1a and justifies exploring high lift as a surrogate for mass flow amplification. The angle of attack for this study is varied from $\alpha = 0°$ to $\alpha = 15°$, which is sufficient to observe the stall of each airfoil considered. Two lines of the same slope are seen on the curve in Figure 2b. The determining factor for which line a particular data point lies on is the location of the stagnation point. For instance, the lift coefficient for the NACA0006 section at $\alpha = 6°$ is nearly equal to that of the modified NACA0006 at

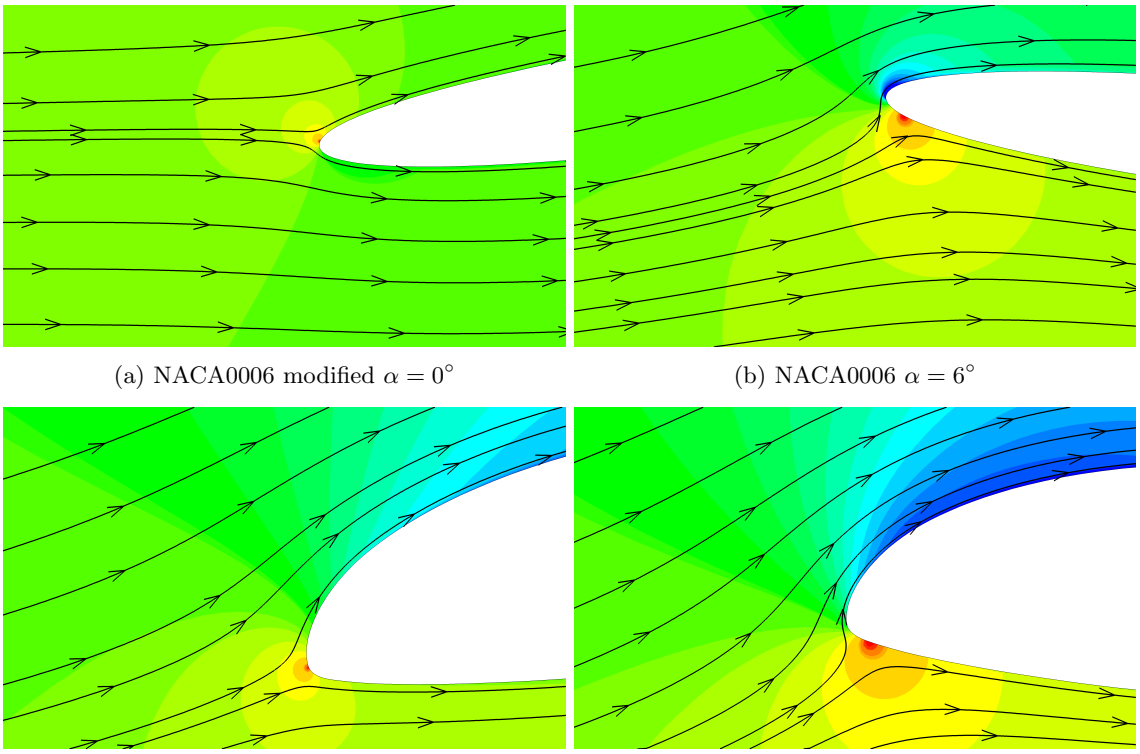

(a) NACA0006 modified $\alpha = 0°$

(b) NACA0006 $\alpha = 6°$

(c) S1223 $\alpha = 4°$

(d) S1223 $\alpha = 15°$

Figure 4: Stagnation point visualizations, contours of pressure.

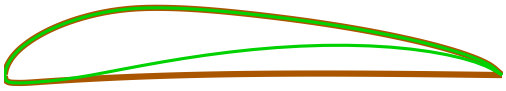

(a) Modified S1223 shape (Original S1223 shape shown in green)

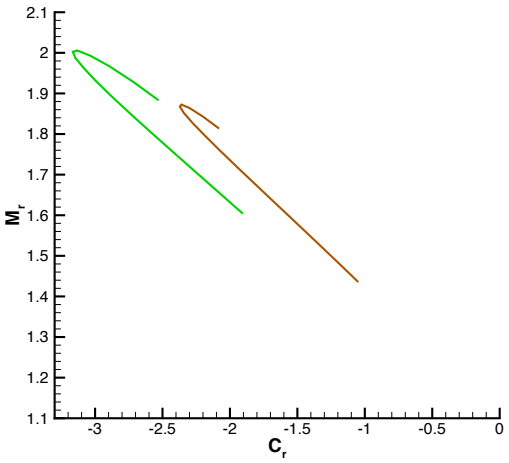

(b) Mass flow amplification M_r vs. radial lift coefficient C_r for S1223 and modified S1223

Figure 5: Analysis of a modified S1223 shape highlights the importance of treating the shroud as an external flow problem

$\alpha = 0°$, yet the NACA0006 induces a greater mass flow. Figures 4a and 4b show contours of pressure and streamlines near the leading edges of these two cases. The interior of the shroud is above the airfoils shown in these plots. In Figure 4a, the stagnation point of the modified NACA0006 is located such that some of the flow approaching the leading edge of the airfoil is diverted downwards and around the shroud. By contrast, in Figure 4b, the location of the stagnation point of the NACA0006 is such that approaching flow is pushed

upwards and into the shroud, increasing the total mass flow. Similarly, Figures 4c and 4d shows the leading edge of the S1223 airfoil at $\alpha = 4°$ and $\alpha = 15°$ respectively. Once again, the radial lift force is nearly equal for these two cases. However there is greater mass flow for $\alpha = 15°$ due to the location of the stagnation point. Of the airfoils considered, the Selig S1223 achieves the greatest mass flow amplification, and for this reason it is selected for 3D analysis in the next section.

The importance of considering an external flow problem is verified by considering a modified version of the S1223 airfoil. Figure 5 shows the modified airfoil with a flattened lower surface, which corresponds to the outer surface of a shroud. The mass flow amplification for this shape is reduced substantially from the original S1223, emphasizing the importance of the shape of the shroud's outer surface in establishing mass capture.

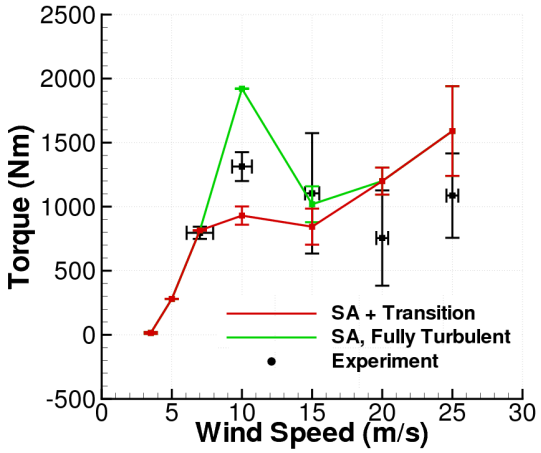

(a) Integrated torque vs. wind speed

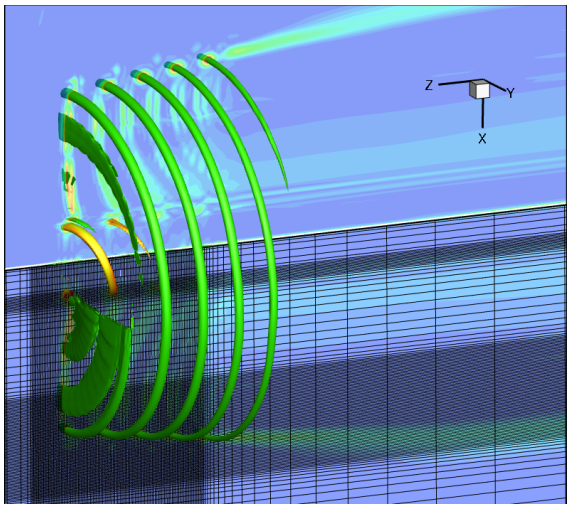

(b) Isocontour of vorticity.

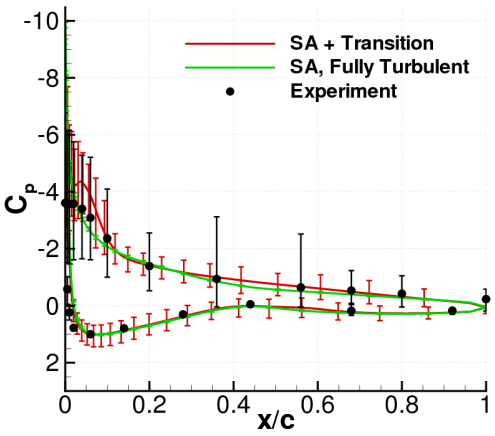

(c) C_p distribution, $r/R = 0.3$, $U_\infty = 10$ m/s

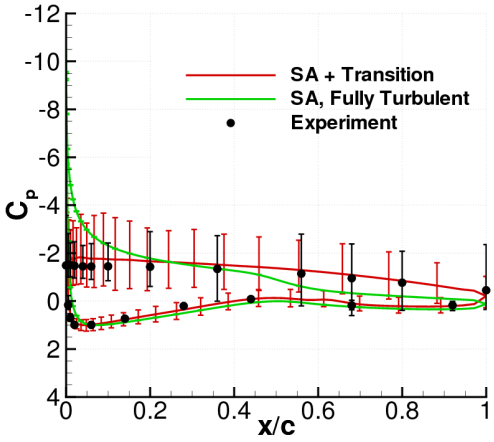

(d) C_p distribution, $r/R = 0.47$, $U_\infty = 10$ m/s

Figure 6: Validation of computational methodology including transition model on NREL Phase VI turbine.

IV. Shrouded wind turbine analysis

A. Validation results

Validation of the methodology used in this study was performed previously,[10] and the computed results of a full 3D wind turbine were compared to those of the NREL Phase VI Unsteady Aerodynamics Experiment.[21] Calculations were performed using the Spalart-Allmaras (SA) turbulence model[18] and the $\gamma - \overline{Re_{\theta t}} - SA$ transition model. The validation study confirmed that the computations predict the behavior of the wind turbine system, and the transition model significantly improves the prediction of pressure forces. Figure 6a plots the integrated torque of the open turbine at various wind speeds. Computed results agree well with experiment, especially at low speeds where the flow is attached. A visualization of a three-dimensional result is shown in Figure 6b, which plots isocontours of vorticity. The shed vortex is seen to persist for several turns of the wake with minimal dissipation. Pressure distributions at two spanwise stations are shown in Figures 6c and 6d for a wind speed of $U_\infty = 10$ m/s. The transition model is seen to capture the pressure distribution more accurately than the fully turbulent assumption at these locations.

B. Baseline (NACA0006) diffuser

For preliminary study, a baseline shroud consisting of a NACA0006 section and a 15° angle of attack, was generated and analyzed. The dimensions for the grids used are $257 \times 51 \times 51$ for the blade and $267 \times 201 \times 49$ for the shroud in the wrap-around, spanwise, and normal directions respectively. Figure 7b shows sections

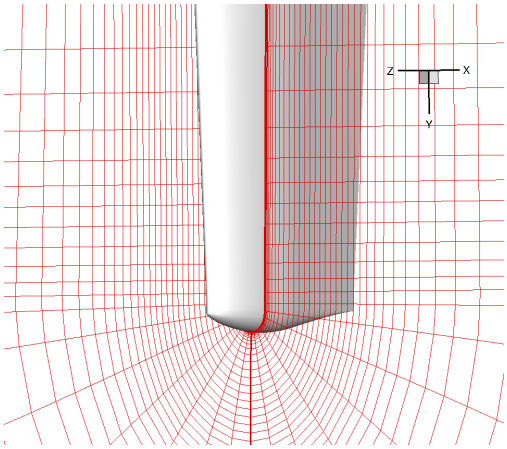

(a) Blade grid

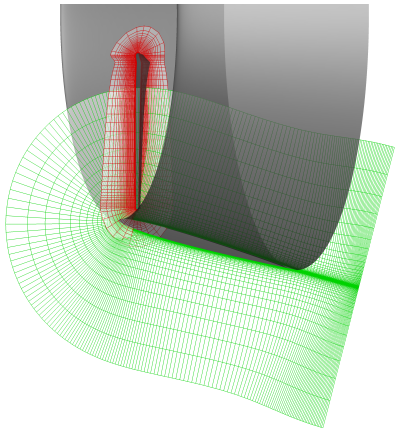

(b) View of blade and shroud

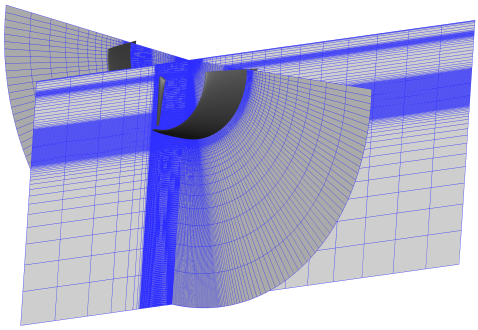

(c) Background grid

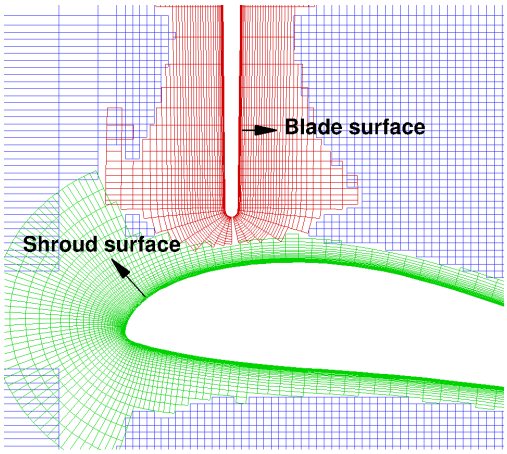

(d) Grid view with field points shown

Figure 7: Overset grids used for 3D computations

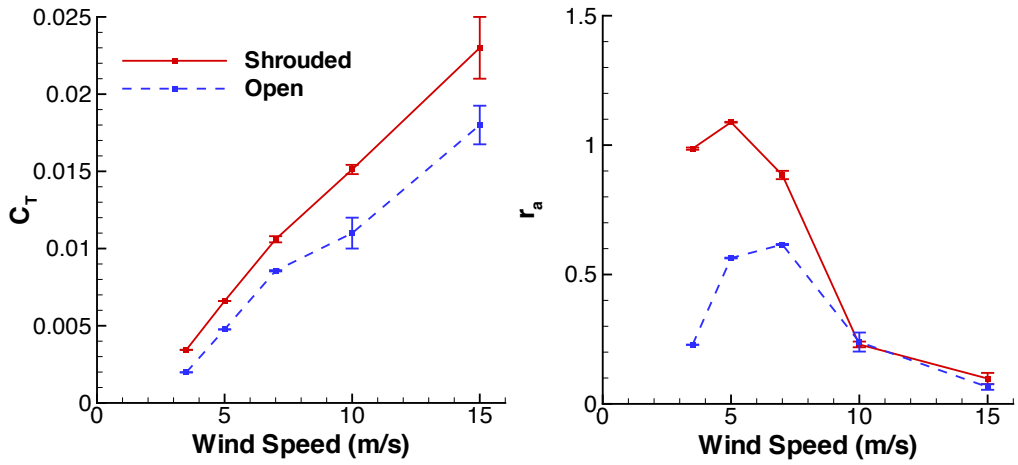

(a) Thrust coefficient

(b) Augmentation ratio

Figure 8: Turbine thrust and augmentation ratio with NACA0006 shroud (ω fixed)

of the blade and shroud grids. A background grid was also used, and has dimensions $201 \times 133 \times 164$ in the azimuthal, radial, and axial directions respectively. The fluid domain is a half-cylinder that extends $2R$ upstream and $6.8R$ downstream and $3.4R$ laterally. Figure 7c shows two planes of the background grid. Periodic boundary conditions are used on the sides of the domain, and characteristic farfield boundary conditions are used on the upstream, downstream, and lateral faces of the cylinder. The azimuthal grid spacing stretches to give fine resolution in a 15° patch in the vicinity of the turbine blade. The equations of motion are solved in the rotating frame.

Results for the baseline diffuser are shown in Figure 8. Unsteady effects are present in the simulations, and error bars are used to indicate maximum and minimum values attained once the solutions reached a periodic steady state. Figure 8a plots the thrust coefficient, defined by

$$C_T = \frac{T}{\rho \pi R^2 V_{tip}^2} \tag{4}$$

where T is the thrust on the turbine blades, R is the turbine radius, and $V_{tip} = \omega R$ is the tip velocity. A commonly used[2,3] measure of DAWT performance is the augmentation ratio, given by

$$r_a = \frac{C_p}{0.593} \tag{5}$$

with

$$C_P = \frac{P}{1/2 \rho V_o^3 \pi R^2}$$

which is simply a ratio of the DAWT power coefficient to the Betz limit. The baseline diffuser is seen to augment both the power and thrust as compared to the bare turbine, with a maximum augmentation ratio of $r_a = 1.09$ at $U_\infty = 5\ m/s$. In this case, power extraction beyond the Betz limit is achieved even with a very simple shroud geometry.

C. High-lift geometry

To examine the effect of a shroud geometry with greater mass flow capture, a second shroud was generated with cross sections of the Selig S1223 airfoil. The grid dimensions and shroud radius were selected to be identical to those of the previous cases. A picture of the shroud grid is shown in Figure 7d. Computational results are shown in Figure 9 alongside the results obtained from the original NACA0006 geometry. The high-lift airfoil greatly improves the performance of the shrouded turbine, yielding a maximum augmentation ratio of $r = 1.91$ at $U_\infty = 5$ m/s. The stall phenomenon that occurs at $U_\infty = 10$ m/s is also evident in Figure 9b, where the performance of the turbine reduces abruptly.

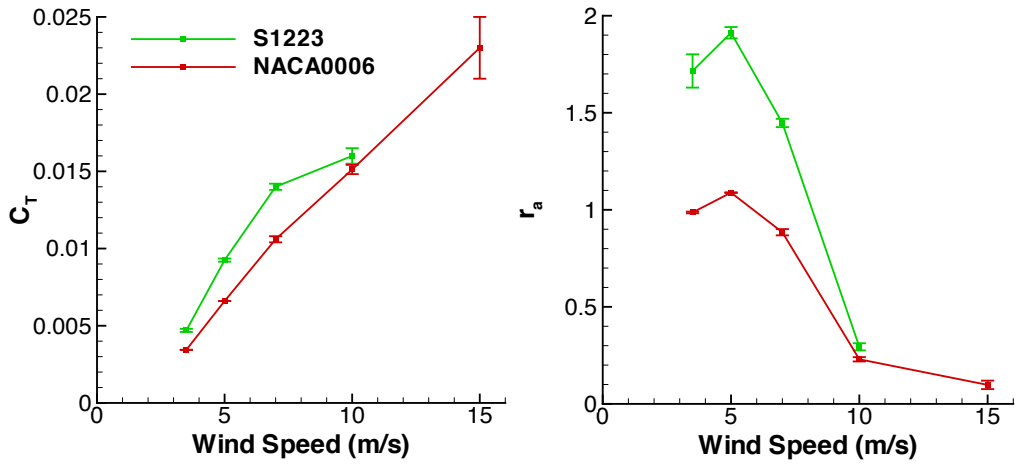

(a) Thrust (b) Augmentation ratio

Figure 9: Thrust coefficient and augmentation ratio for NACA006 shroud and Selig S1223 shroud (ω fixed)

The effect of the shrouds on the spanwise distribution of loads on the turbine blade is shown in Figures 10 and 11, which plot the incremental loads at each spanwise location. Two wind speeds are shown, $U_\infty = 5$ m/s, where peak augmentation is obtained, and $U_\infty = 7$ m/s, which marks the onset of separation for the shrouded cases. At $U_\infty = 5$ m/s, where the turbine is more efficient in augmenting the power output, the increase in loading is smooth, peaking near $r/R = 0.9$. At $U_\infty = 7$ m/s, the force coefficients which are smooth for the open rotor begin to deteriorate from the outboard portion of the blade. Partial separation is present in these regions.

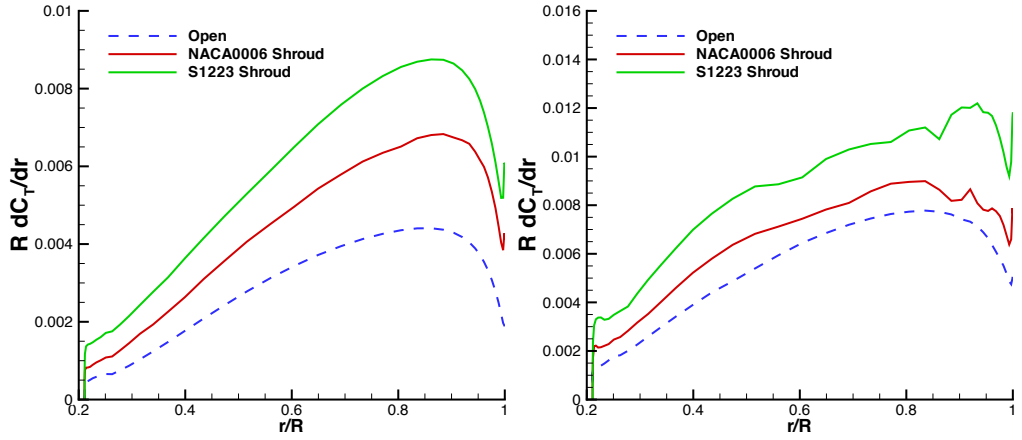

(a) $U_\infty = 5$ m/s (b) $U_\infty = 7$ m/s

Figure 10: Spanwise thrust coefficient

To further investigate the irregularities seen in the outboard portion of the blade, Figure 12 shows contours of pressure and streamlines for a cross section taken at $r/R = 0.7$. Separation is indeed present in both shrouded cases. The overall pressures are lower in the cases where the shroud accelerates the fluid, and the local angle of attack experienced by the section is higher as well.

D. Flow field

The evolution of fluid velocity as it passes through the turbines is examined in Figure 13, where azimuthally averaged velocity profiles are shown at 6 axial stations. The case where $U_\infty = 5$ m/s is selected for this analysis, as it corresponds to the greatest power augmentation. Upstream of the turbine, at z/R=2.16 (red),

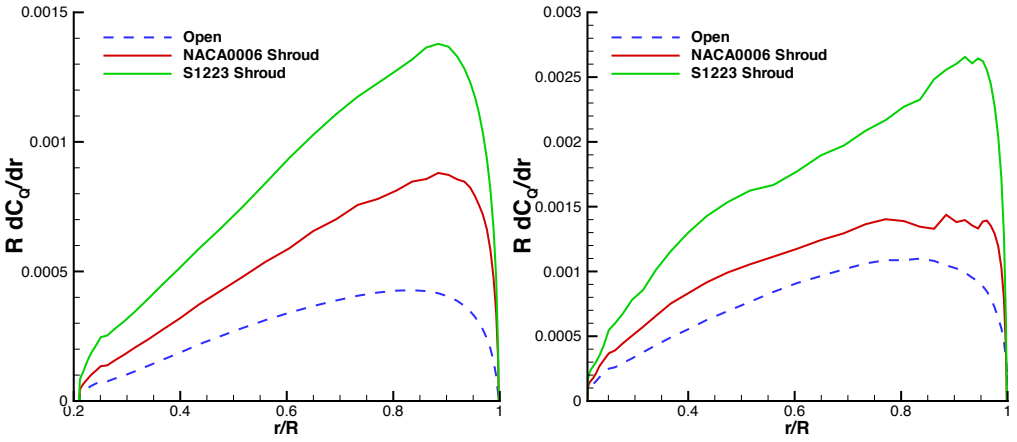

(a) $U_\infty = 5$ m/s (b) $U_\infty = 7$ m/s

Figure 11: Spanwise torque coefficient

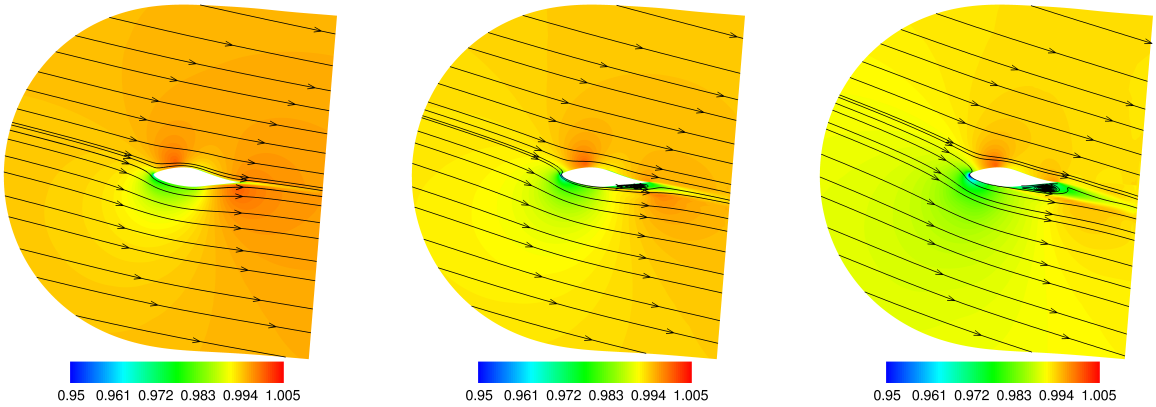

(a) Open (b) NACA0006 (c) S1223

Figure 12: Contours of p/p_∞ at slices of turbine blade at $r/R = 0.7$, $U_\infty = 7$ m/s

the velocity profiles are constant at the freestream value of 5 m/s. At $z/R = 0.47$ (orange), a deficit is seen in the wake of the open turbine corresponding to an expansion of incoming streamlines. At this axial station, a peak is seen in the vicinity of the shroud (near $r/R = 1$) in Figures 13b and 13c, and the flow acceleration due to the shroud prevents an upstream wake deficit. In fact, the S1223 shroud accelerates the air enough that the incoming velocity is greater than the freestream across the entire span of the turbine. Very close to the plane of the turbine, at $z/R = 0.01$ (gold), the wake of the open rotor has decelerated halfway to the downstream wake, agreeing with the result from actuator disk theory. Both shrouds, on the other hand, alleviate this wake deficit. Downstream (blue and purple), the wake deficits are much larger for the shrouded turbines due to both an increase in turbine thrust and momentum extraction by the shroud itself. The shrouded turbine wakes also expands farther laterally in this downstream region.

Contours of normalized pressure along the turbine blades are shown in Figure 14. The differences between the cases are most pronounced on the leeward surface. In the plots on the left, lower pressures are seen towards the outer region of the blade in the shrouded cases, where the effect of the shroud suction peak is felt most strongly. On the right, contours of skin friction coefficient c_f are shown. Streamlines indicating the flow direction immediately adjacent to the surface are superimposed on these plots. For the open turbine, the flow is completely attached and laminar across the entire turbine surface. For the shrouded cases however, a laminar separation bubble is seen as a blue stripe across the blades. At this location, the skin friction is negative and locally the flow is in the reverse direction. This phenomenon, which was previously observed

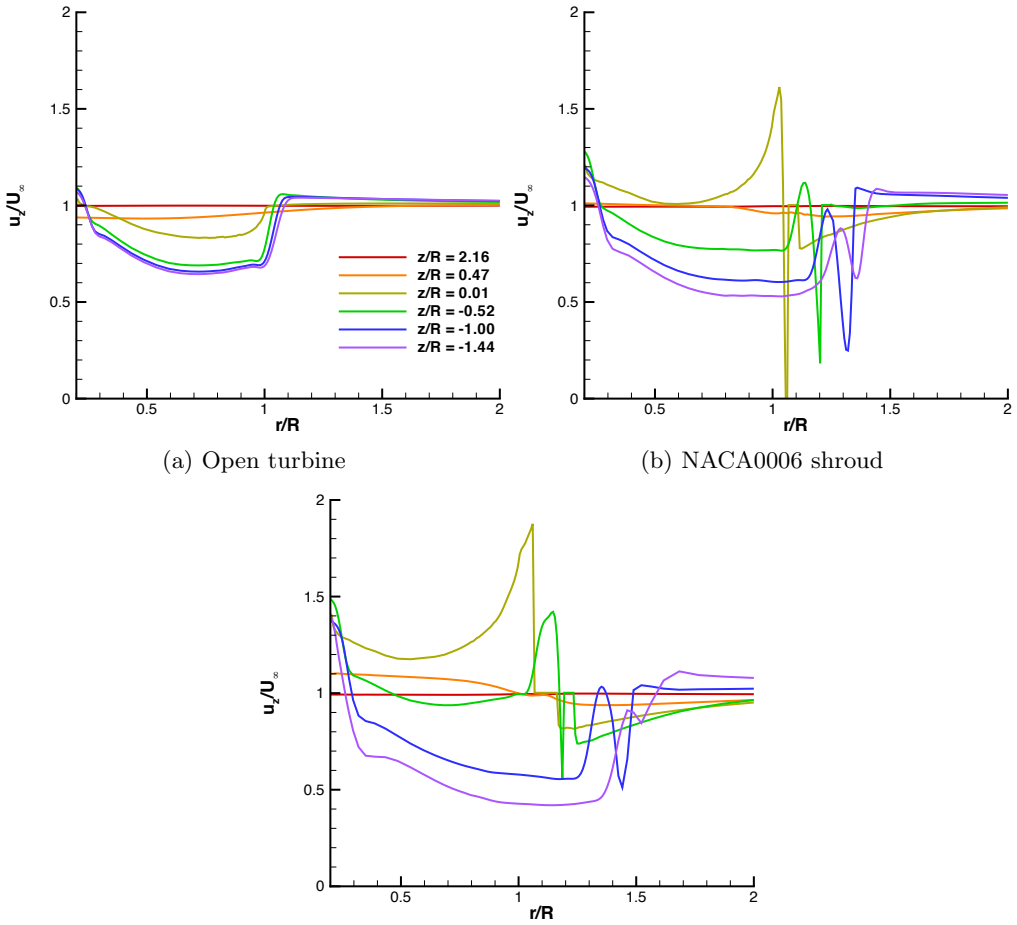

(a) Open turbine

(b) NACA0006 shroud

(c) S1223 shroud

Figure 13: Azimuthally averaged velocity distribution, $U_\infty = 5$ m/s

to occur for the open turbine at higher wind speeds, occurs at the low speed of $U_\infty = 5$ m/s due to the flow acceleration of the shrouds.

Interesting features are seen in the interaction between the turbine wake and the shroud. Figures 15 and 16 show contours of vorticity taken at an azimuthal station just as the blade passes by. Downstream of the turbine, several passes of the helical turbine wake appear in close proximity to the shroud, revealing the expansion of the helix within the shroud. The vorticity shed from the shroud boundary layer oscillates with the passing wake. The fluid in the boundary layer decelerates toward pressure recovery but is intermittently reenergized by the passing turbine vortex. This phenomenon promotes attached flow, and is quite beneficial in preventing stall on the shroud inner surface.

A further visualization of the flow around the shroud is shown in Figures 17 and 18. The pressure coefficient along the shroud is plotted for wind speeds of $U_\infty = 5$ m/s and $U_\infty = 10$ m/s respectively. In each case, the pressure coefficient is shown at various azimuthal positions as thin lines. An average over all azimuthal coordinates is shown with the thick line. The solution of a 2D axisymmetric simulation is shown as well for comparison. Note that the axisymmetric solutions did not make use of the transition model and instead assume fully turbulent flow. The location where the azimuth $\theta = 90°$ corresponds to the location of the turbine blade. Particularly in the case with $U_\infty = 5$ m/s, a large peak is seen at this location. The pressure is seen in each case to drop lower than predicted by the axisymmetric simulation owing to the acceleration of the boundary layer by the turbine wake, is readily visible as oscillations in these plots.

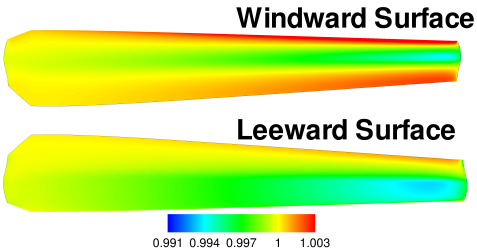

(a) Open turbine, contours of p/p_{inf}

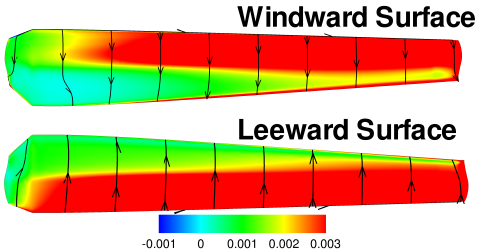

(b) Open turbine, contours of c_f

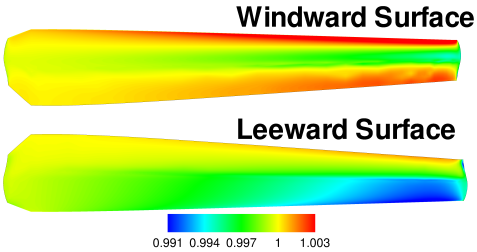

(c) NACA0006 shroud, contours of p/p_{inf}

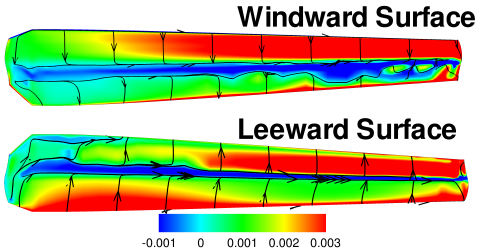

(d) NACA0006 shroud, contours of c_f

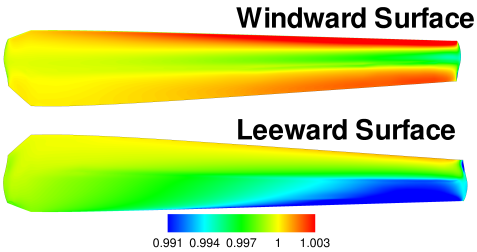

(e) S1223 shroud, contours of p/p_{inf}

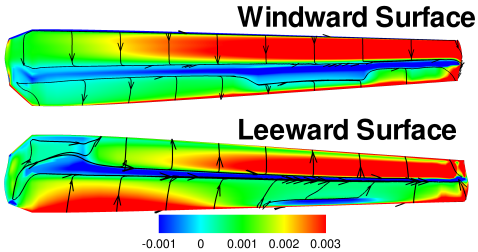

(f) S1223 shroud, contours of c_f

Figure 14: Contours of pressure and skin friction, $U_\infty = 5$ m/s

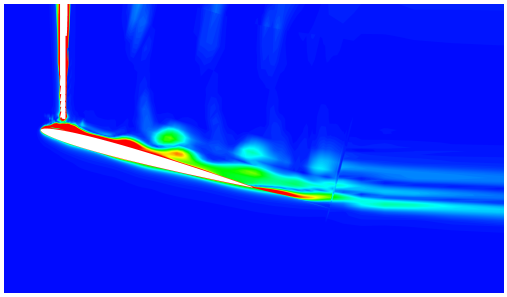

(a) $U_\infty = 5$ m/s

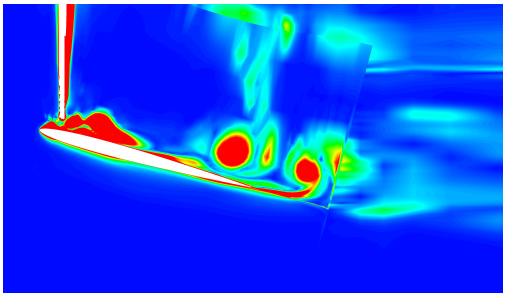

(b) $U_\infty = 10$ m/s

Figure 15: Contours of vorticity magnitude for NACA0006 shroud

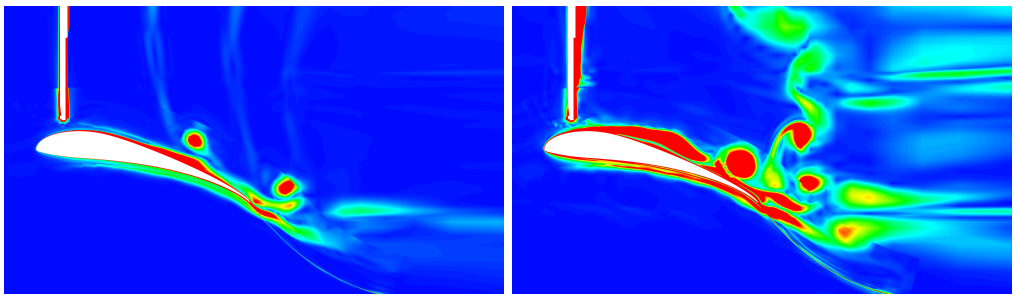

(a) $U_\infty = 5$ m/s (b) $U_\infty = 10$ m/s

Figure 16: Contours of vorticity magnitude for S1223 shroud

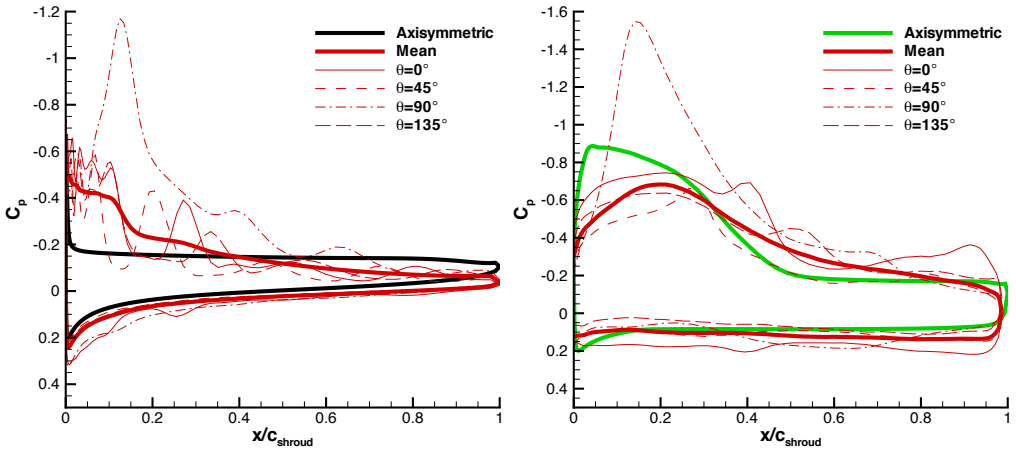

(a) NACA0006 (b) S1223

Figure 17: Shroud pressure coefficient, $U_\infty = 5$ m/s

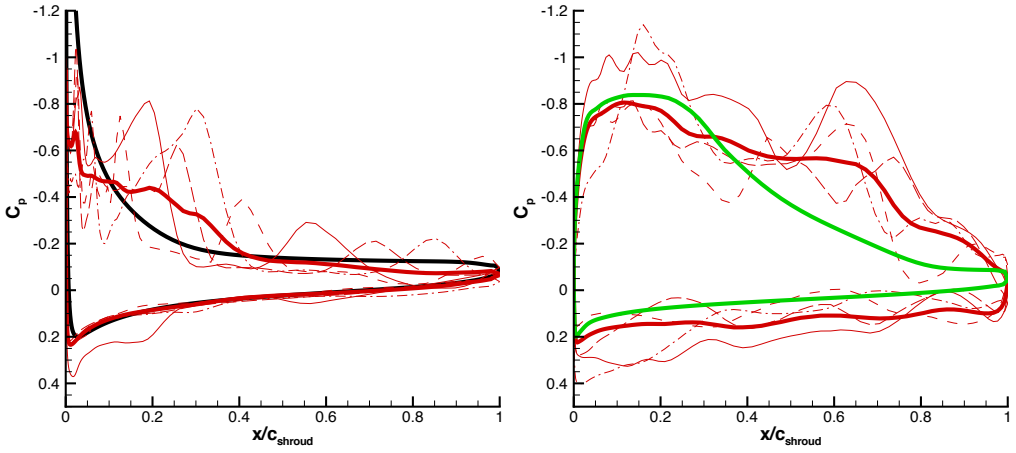

(a) NACA0006 (b) S1223

Figure 18: Shroud pressure coefficient, $U_\infty = 10$ m/s

E. Matching tip speed ratio

In practice, it is typically desirable to select a wind turbine's angular velocity ω to match the rate at which the gearbox and power generator perform optimally. In Figure 8b, the power produced by the shrouded turbine while maintaining a fixed ω is seen to collapse onto that of an open turbine abruptly at $U_\infty = 10$ m/s. At and beyond this speed, there is separation on the blade surface owing to the higher angle of attack experienced by each blade section. The geometric angle of attack is given by

$$\alpha(r) = \phi(r) + \tan^{-1}\left(\frac{1}{\lambda}\frac{R}{r}\right) \tag{6}$$

where $\phi(r)$ is the twist of the blade. Inspection of this relation confirms that increasing wind speed while maintaining a rotation rate ω will decrease λ and increase the angle of attack at all spanwise locations. In order to investigate the aerodynamic performance of the shrouded turbine in the absence of changes in geometric angle attack, simulations were rerun maintaining a fixed value of λ. The results are shown in Figure 19. For the purpose of this study, a value of $\lambda = \lambda_0 \approx 5.42$ is selected, which matches the value attained at $V_\infty = 7$ m/s of Figure 8b. From Figure 19b, it is evident that by maintaining the original angle of attack, gains in power augmentation are achieved at higher wind speeds in the shrouded configuration.

The flow solution of a rotating system with a given geometry depends on three non-dimensional groups. For the problem under consideration, one choice for these groups is freestream Reynolds number Re, freestream Mach number M_∞, and the tip speed ratio λ. For a wind turbine that can be accurately modelled using inviscid and incompressible flow assumptions, the dependence of the flow solution on these parameters collapses to a dependence on λ only. From Figure 19, it is seen that the force coefficients associated with the bare turbine remain nearly constant as U_∞ increases. This reflects the fact that the wind turbine is a low-speed lift-driven machine for which compressibility and viscous effects play a small role. By comparison, a large change is seen in the performance of the shrouded turbine across the same range of wind speeds. This indicates that the parameter λ alone is not sufficient to capture the behavior of the shrouded turbine. Compressibility effects in this problem are minimal. Thus, the difference in behavior between the shrouded and unshrouded turbines at fixed λ are due to a greater sensitivity to Reynolds number for the shrouded turbine. More specifically,

$$\left(\frac{\partial C_{P,d}}{\partial Re}\right)_{\lambda=\lambda_0} > \left(\frac{\partial C_{P,b}}{\partial Re}\right)_{\lambda=\lambda_0} \tag{7}$$

where, following the notation of Hansen,[4] $C_{P,d}$ is the power coefficient of a DAWT, $C_{P,b}$ is the power coefficient of the bare turbine. One implication of this is that an inviscid solver validated against bare turbine is insufficient for predicting the behavior of a DAWT. Considering the Reynolds numbers involved and the patterns observed on the turbine blades in Figure 14, the effect of transition in particular plays a critical role in the behavior of these systems.

V. Conclusions and future work

An investigation of airfoil sections for shrouds of shrouded wind turbines has been performed. Of a number of airfoil shapes considered for shroud cross sectional profiles, the Selig S1223 attains the greatest amplification of mass flow. Three-dimensional analysis of full shrouded turbine systems verify the benefit of increased mass flow through the plane of the turbine. Power extraction up to 90% beyond the Betz limit is achieved. The improvement in power extraction beyond the bare turbine is substantial; the NACA0006 shroud improves power over the bare turbine by a factor of 1.93 and the S1223 improves it by a factor of 3.39 at $U_\infty = 5$ m/s. These results further support the utility of the shrouded wind turbine as a device that can be used effectively at low cut-in speeds and offer promise to substantially improve the energy capture when compared to conventional wind turbines.

Based on the preceding analysis, the following conclusions are drawn regarding the design of a shrouded turbine:

- A low R_s/c ratio is desired, which places a constraint on the practical size of a shrouded turbine.
- In the absence of a turbine, mass flow amplification through a shroud increases approximately linearly with radial force, and nonlinear behavior occurs as the stagnation point moves from the interior to the exterior side of the shroud.

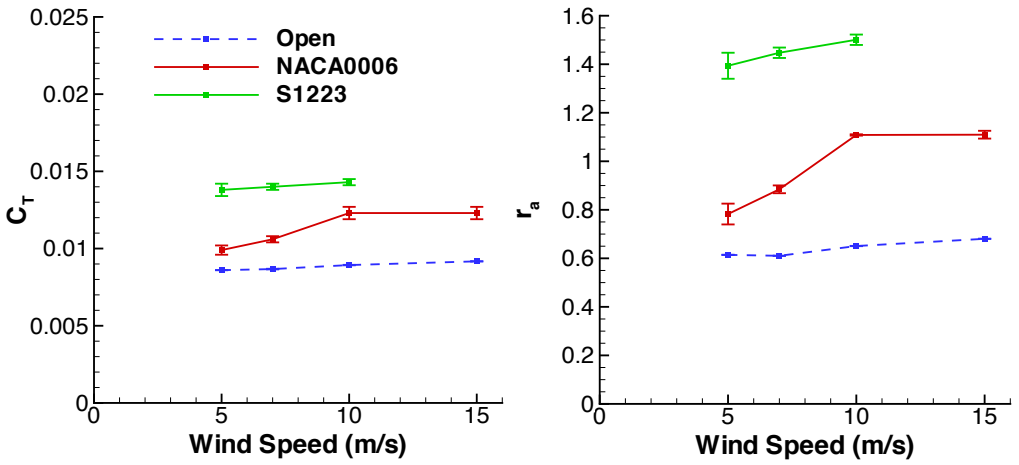

(a) Thrust Coefficient (b) Augmentation ratio

Figure 19: Shrouded turbine performance at fixed λ

- The benefit of a shroud is maximum at freestream velocities where the flow over the bare turbine is fully laminar. The presence of the shroud hastens transition and separation.
- The wake of a shrouded turbine expands more rapidly than an open turbine and can be tailored to promote maximum power extraction.
- Reynolds number and transitional flow has a larger effect on the behavior of a shrouded wind turbine than for open turbines and should be accounted for in analysis whenever feasible.

The above considerations provide insight for both the analysis and design of both the shroud and the turbine of a shrouded turbine. Future work will employ an optimization strategy to design a shrouded turbine with a continued detailed focus on fluid physics.

Acknowledgement

This work is partially supported by the DoD NDSEG fellowship and by the DoE ASCR program on Fluid/Structure interactions in Wind Turbine Applications at Stanford University.

References

[1]Lilley, G. M. and Rainbird, W. J., "A preliminary Report on the Design and Performance of a Ducted Windmill, Report 102," *College of Aeronautics*, 1956.

[2]Gilbert, B. L. and Foreman, K. M., "Experiments With a Diffuser-Augmented Model Wind Turbine," *Journal of Energy Resources Technology*, Vol. 105, 1983.

[3]Igra, O., "Research and Development for Shrouded Wind Turbines," *Energy cons. & Mgmt*, Vol. 21, 1981, pp. 13–48.

[4]Hansen, M. O. L., Sørensen, N. N., and Flay, R. G. J., "Effect of Placing a Diffuser Around a Wind Turbine," *Wind Energy*, Vol. 3, 2000.

[5]Werle, M. J. and Presz Jr., W. M., "Ducted Wind/Water Turbines and Propellers Revisited," *Journal of Propulsion and Power*, Vol. 24, No. 5, 2008.

[6]Jamieson, P., "Beating Betz: Energy Extraction Limits in a Constrained Flow Field," *Journal of Solar Energy Engineering*, Vol. 131, 2009.

[7]Ohya, Y. and Karasudani, T., "A Shrouded Wind Turbine Generating High Output Power with Wind-lens Technology," *Energies*, Vol. 131, 2010.

[8]Abe, K. and Ohya, Y., "An investigation of flow fields around flanged diffusers using CFD," *Journal of Wind Engineering and Industrial Aerodynamics*, Vol. 92, 2004.

[9]van Bussel, G., "The science of making more torque from wind: Diffuser experiments and theory revisited," *Journal of Physics: Conference Series*, Vol. 75, 2007.

[10]Aranake, A., Lakshminarayan, V., and Duraisamy, K., "Assessment of Transition Model and CFD Methodology for Wind Turbine Flows," 42^{nd} *AIAA Fluid Dynamics Conference and Exhibit*, New Orleans, LA, June 2012.

[11]Medida, S. and Baeder, J., "Numerical Prediction of Static and Dynamic Stall Phenomena using the $\gamma - \overline{Re_{\theta t}}$ Transition Model," *American Helicopter Society* 67^{th} *Annual Forum*, Virginia Beach, VA, May 2011.

[12]Lakshminarayan, V. K. and Baeder, J. D., "Computational Investigation of Microscale Shrouded Rotor Aerodynamics in Hover," *Journal of the American Helicopter Society*, 2011, 56, 042002.

[13]Lakshminarayan, V. K., "Computational Investigation of Micro-Scale Coaxial Rotor Aerodynamics in Hover," *Ph.D. dissertation, Department of Aerospace Engineering*, 2009.

[14]Buelow, P. E. O., Schwer, D. A., Feng, J., and Merkle, C. L., "A Preconditioned Dual-Time, Diagonalized ADI scheme for Unsteady Computations," *13th AIAA Computational Fluid Dynamics Conference*, Snowmass Village, CO, June 1997.

[15]Pandya, S. A., Venkateswaran, S., and Pulliam, T. H., "Implementation of Preconditioned Dual-Time Procedures in OVERFLOW," *41st AIAA Aerospace Sciences Meeting and Exhibit*, Reno, NV, January 2003.

[16]Pulliam, T. and Chaussee, D., "A Diagonal Form of an Implicit Approximate Factorization Algorithm," *Journal of Computational Physics*, Vol. 39, No. 2, 1981, pp. 347–363.

[17]Turkel, E., "Preconditioning Techniques in Computational Fluid Dynamics," *Annual Review of Fluid Mechanics*, Vol. 31, 1999, pp. 385–416.

[18]Spalart, P. R. and Allmaras, S. R., "A One-equation Turbulence Model for Aerodynamic Flows," *30th AIAA Aerospace Sciences Meeting and Exhibit*, Reno, NV, January 1992.

[19]Lee, Y., "On Overset Grids Connectivity and Vortex Tracking in Rotorcraft CFD," *Ph.D. dissertation, Department of Aerospace Engineering*, 2008.

[20]Selig, M. S. and Guglielmo, J. J., "High-Lift Low Reynolds Number Airfoil Design," *Journal of Aircraft*, Vol. 34, No. 1, 1997.

[21]Hand, M. M., Simms, D., Fingersh, L. J., Jager, D. W., Cotrell, J. R., Schreck, S., and Lawood, S. M., "Unsteady Aerodynamics Experiment Phase VI: Wind Tunnel Test Configurations and Available Data Campaigns," *NREL/TP-500-29955*, 2001.